

Experimental study on thermal performance of ultra-high performance concrete with coarse aggregate at high temperature

Congcong Xue ^{a,c}, Min Yu ^{a,b,*}, Haoming Xu ^a, lihua Xu^a, Mohamed Saafi^c, Jianqiao Ye ^{c*}

^a School of Civil Engineering, Wuhan University, Wuhan, Hubei Province, 430072, China.

^b Research Center of Urban Disasters Prevention and Fire Rescue Technology of Hubei Province, Wuhan, Hubei Province, 430072, China.

^c Department of Engineering, Lancaster University, Lancaster, LA1 4YR. UK.

ABSTRACT: Ultra-high performance concrete (UHPC) exhibits superior mechanical and durability performance with very high compressive strength. Compared with ordinary concrete, it is more environmentally friendly and has the great potential to be a practical solution to improve the sustainability of infrastructure. This study focuses on examining thermal properties of UHPC with coarse aggregates (CA-UHPC) subjected to temperature ranged from 20°C ~900°C, including changes in macro and micro morphology before and after high temperatures, thermal conductivity, mass loss, specific heat and thermal expansion. The effects of high temperature, coarse aggregate and steel fiber content on the thermal performance of the material will be evaluated both qualitatively and quantitatively. Experimental results show that high temperature greatly affects thermal properties of CA-UHPC. Coarse aggregates also have a considerable influence on the thermal properties. Steel fibers, however, have little effect on the thermal properties. Based on the test results, meso calculation formulas are proposed to predict the thermal properties, which can be used in the design of structural components made of CA-UHPC.

Keywords: CA-UHPC; high temperature; thermal parameters; coarse aggregates; steel fibers

1 Introduction

Compared with ordinary concrete, Ultra-high performance concrete (UHPC) is a new type of sustainable and environment-friendly material that has a high compressive strength, tensile ductility and toughness. Reactive powders and fibers are normally added to the mixture to achieve the design requirements. The use of reactive powders can fill the fine pores, resulting in a super dense material structure. Adding steel fibers to the mixture increases the capacity to sustain flexural and tensile loads, even after initial cracking, thus achieves higher toughness. Obviously, applications of UHPC will promote “do more with less” and “build to last”, resulting in significant reduction of embodied CO₂ in concrete.

In the past few decades, significant advances in the research of steel reinforced concrete structures in fire have been made through rigorous testing, both small and large scale, which led to the development of reliable modelling and analytical techniques. These techniques were developed based on improved understanding of

* Corresponding authors: ceyumin@whu.edu.cn (M. Yu); j.ye2@lancaster.ac.uk (J.Ye)

high-temperature thermal performance of structural components made of normal strength concrete. Apparently, with the increase usage of UHPC in a broad range of infrastructure designs, thermal performance of UHPC has now become a topic that requires urgent attention.

Most of the work in the literatures on concrete focused on factors such as temperature, the type and content of aggregates and fibers ^[1, 2]. For example, Wang^[3]、Li^[4]、Wang^[5] and Zhang^[6], et al. studied the changes in thermal properties of different types of concrete at elevated temperatures, and established the relationships between thermal parameters and temperature. Ju et al.^[7] explained the mechanism of change in thermal performance of reactive power concrete (RPC) at elevated temperatures and developed analytical expressions of thermal parameters in relation to temperature and steel fiber content. EC2^[8] and ASCE^[9] provide empirical formulas for thermal conductivity, specific heat, density and thermal expansion of normal strength concrete (NSC) under high-temperature. Zheng et al.^[10] studied temperature dependent thermal parameters of RPC by curve fitting using experiment data and inverse finite element. It was found that thermal conductivity of RPC was higher than that of high strength concrete (HSC) and NSC. Kim^[11] and Zhang^[12] et al. conducted experiments to study the influence of the type and content of coarse aggregates in NSC on the thermal conductivity at room temperature. They found that volume fraction of coarse aggregates was the main factor, and was positively correlated with thermal conductivity. Corinaldesi et al.^[13] tested thermal conductivity of ultra-high performance fiber concrete at room temperature. Kodur^[14-17] and Zheng et al. ^[10] tested concrete and RPC at elevated temperatures. They found that fiber content (within 2%) had no obvious effect on the thermal conductivity of concrete and RPC. Some researchers, including Emamel^[18], Siddiqui^[19], Nahhas^[20], and Vigroux^[21] et al. conducted detailed studies on thermal expansion of concrete. These studies have shown that thermal expansion is closely related to the composition and content of a concrete material.

The above-mentioned researches have provided fundamental understanding of the thermal performance of concrete at normal and high temperatures. However, to the authors' best knowledge, reports on testing and predicting thermal parameters of CA-UHPC are still hardly found, especially at high temperatures. The mix proportion of CA-UHPC is significantly different to that of other types of concrete, which is, undoubtedly, a cause for concern in promoting applications of this new material. To address this concern, thermal properties of CA-UHPC at high temperature need to be further examined. In this study, systematical tests and detailed investigations on the performance of CA-UHPC subjected to high temperatures are carried out. Thermal conductivity, mass loss, specific heat and thermal expansion of CA-UHPC at elevated temperatures are measured experimentally. The effects of high temperature, coarse aggregate and steel fiber content on the thermal performance of CA-UHPC are studied, including changes in the internal physical and chemical structures of the

material. Finally, simplified calculation formulas are proposed to predict the temperature dependent thermal parameters.

2 Test preparation

2.1 Materials and mix ratio

The raw materials of CA-UHPC include cementitious materials (cement, silica fume and fly ash, etc), quartz sand, coarse aggregates, copper plated steel fibers, water, and water reducer. The grade of ordinary Portland cement is 52.5. The silica content in the silica fume is about 90% with an average particle size of nanometer scale, thus, can fill the micro- and nano-scale pores in the cement and other components. The Grade I fly ash contains more than 60% silica and alumina, the use of which can improve workability of concrete and contribute to environmental protection. The coarse aggregates are basalt with particle size of 5mm~10mm. The straight copper-plated micro-wire steel fibers has a length of $12\text{ mm} \pm 1\text{ mm}$ and a diameter of $0.20\text{mm} \sim 0.25\text{ mm}$. The addition of coarse aggregates and steel fibers help to reduce autogenous shrinkage of CA-UHPC at early-age. Tap water is used. The water-reducing agent is a high-performance liquid polycarboxylate superplasticizer.

The CA-UHPC is composed of RPC matrix and coarse aggregates. The volume fractions of coarse aggregates in the CA-UHPC are 0, 10%, 20%, and 30%, respectively. The volume fractions of steel fibers are 0, 1%, 2%, and 3%, respectively. Taking the CA-UHPC with a coarse aggregate content of 20% and a steel fiber content of 2% as the benchmark mix ratio, a total of 7 UHPCs with different mix ratios are designed for the experiment. The sample number and mix proportion of CA-UHPC are shown in Table 1.

Table 1 Mix ratio of CA-UHPC (by mass ratio)

Sample ID	Cementitious material	Cement	Silica fume	Fly ash	Water	Water reducing agent	Quartz sand	Steel fibers	Coarse aggregates
C0S02	1	0.80	0.15	0.05	0.16	0.03	1.37	0.18(2%)	0.00(0%)
C10S02	1	0.80	0.15	0.05	0.16	0.03	1.37	0.18(2%)	0.32(10%)
C20S02	1	0.80	0.15	0.05	0.16	0.03	1.37	0.18(2%)	0.72(20%)
C30S02	1	0.80	0.15	0.05	0.16	0.03	1.37	0.18(2%)	1.23(30%)
C20S0	1	0.80	0.15	0.05	0.16	0.03	1.37	0.00(0%)	0.70(20%)
C20S01	1	0.80	0.15	0.05	0.16	0.03	1.37	0.08(1%)	0.71(20%)
C20S03	1	0.80	0.15	0.05	0.16	0.03	1.37	0.27(3%)	0.73(20%)

In Table 1, The sample ID in the first column shows the volume ratios of coarse aggregates and steel fibers, e.g., C20S02 means that the mixture has 20% coarse aggregates (C20) and 2% steel fibers (S02) in volume. The percentages in the brackets of the last two columns are the volume fractions of steel fibers and coarse aggregates,

respectively.

2.2 Preparation of samples

The pouring process of the CA-UHPC mainly includes initial preparation, weighing and mixing of raw materials, pouring and curing. The fluidity of the fresh CA-UHPC is tested first according to GB/T 5008-2016. The fresh CA-UHPC is then poured into a slump cone with an upper diameter of 100 mm, a lower diameter of 200 mm and a height of 300 mm. The cone is lifted vertically upwards and the slump of the CA-UHPC is measured. The range of the slump of the samples in Table 1 is between 220mm~320mm. After the mixture is poured into the mold, it is placed on a shaking table to vibrate until the surface is pulped. After covering with plastic film and standing for 48hrs, the sample is demolded and cured. The preparation and processing of the samples are illustrated in



Figure 1.

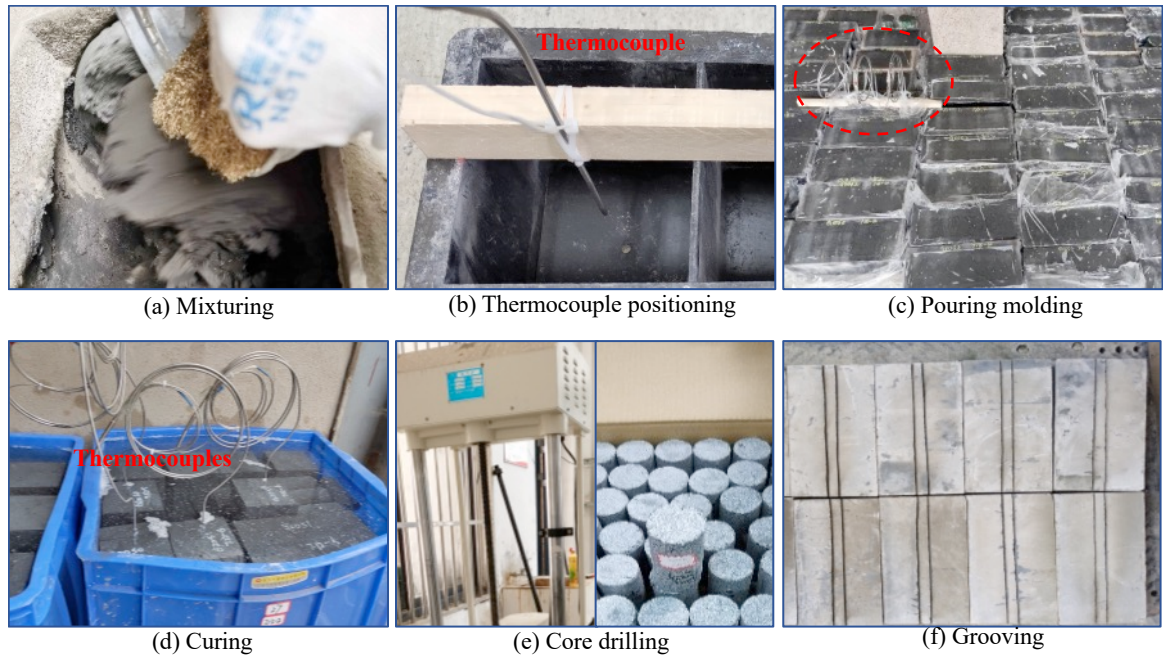


Figure 1 Manufacturing process of specimens

Cubic specimens of side length 100 mm are made to measure the mass loss and specific heat of the CA-UHPC. For thermal conductivity test, specimens of $230\text{mm} \times 114\text{mm} \times 64\text{mm}$ are used according to GB/T 5990-2006 and are grooved and polished



Figure 1(f)). A thermocouple is embedded in the center of the specimen for specific heat test, as shown in



Figure 1(b)~(d). The cylindrical specimens of $\text{Ø}50 \text{ mm} \times 100 \text{ mm}$ shown in Figure 1(e) are used for thermal expansion test.

2.3 Experiment design and preparation

Thermal conductivity: For materials such as concrete, the commonly used measurement methods of thermal conductivity include steady-state method, transient hot wire method, laser flash diffusion coefficient method and transient plane source method^[22-24]. Taking into account the time required for the tests and other conditions, the transient parallel hot wire method is chosen in this study. Ten target temperatures, namely 20°C , 100°C , 200°C , 300°C , 400°C , 500°C , 600°C , 700°C , 800°C and 900°C , are chosen to study the material properties at each of them.

Mass loss: After weighing the specimen, it is placed into a high-temperature electric furnace at room temperature. After the furnace reaches each of the target temperatures (20°C , 100°C , 300°C , 500°C , 700°C , and 900°C), the temperature is maintained for 3hrs before cooling. The sample is then removed from the cooled furnace for immediate weighing. This process is repeated for all the 6 target temperatures.

Specific heat: There are mainly three test methods to directly measure specific heat, i.e., the conventional measurement method, differential thermal analysis (DTA) and differential scanning calorimetry (DSC). The above methods work well only on very small samples of 1 mg to 10 mg. However, concrete is a non-uniform material containing coarse aggregates of, e.g., 5~10 mm in this study. The weight of such a single coarse aggregate is greater than 300mg. If the specific heat is measured directly, it is very likely to have inconsistent test results. Alternatively, the problem is dealt with an inverse, rather than forward, problem solving technique. From the earliest research on inverse heat transfer problem^{[25][26][27]}, it was found that the solution of an heat

equation satisfies the conditions of existence, uniqueness and stability, thus the solution of specific heat from an inverse process must also be unique and stable.

To find the specific heat of the material using inverse solution, the time dependent temperature curve of the central point of a sample is produced first based on the collected experiment data of the thermocouple. A three-dimensional finite element heat transfer model is then developed to simulate the laboratory test to obtain a temperature-time curve that is most close to the test one by searching the optimal value of specific heat using the gradient method.

Thermal expansion: Thermal expansion is an important property in predicting thermal stress of a material at high temperatures. There have been many studies on using various test equipment^[28-30]. In this paper, the sample is heated from normal temperature to 900 °C at the rate of 3 °C/min, and kept at 50 °C, 100 °C, 200 °C, 300 °C, 400 °C, 500 °C, 600 °C, 700 °C, 800 °C and 900 °C, respectively, for 90 min to ensure that the temperature of the sample is uniform. Thermal expansion of the sample is recorded continuously by an electronic dial indicator.


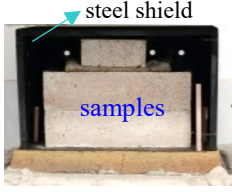
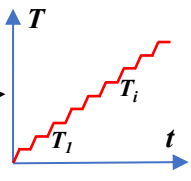
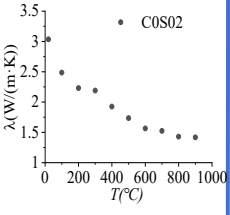
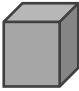
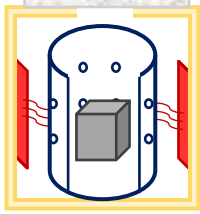
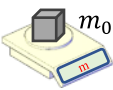
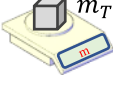
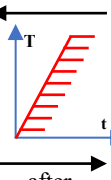
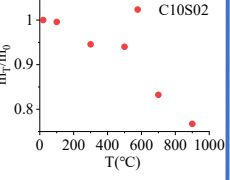
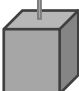
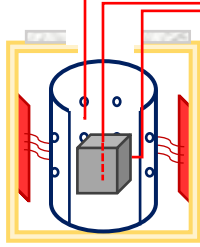

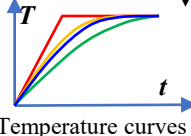
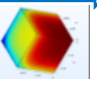
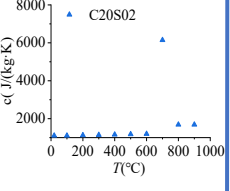

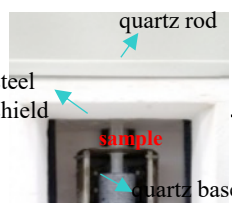
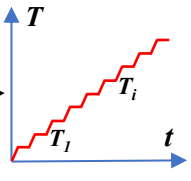
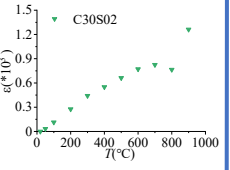
Item	Specimen	Set-up	Method	Results
Thermal conductivity	 <p>Brick: L:230mm W:114mm H:64mm</p>	 <p>steel shield samples</p> <p>Furnace chamber Continuous graded heating</p> 	$\lambda = \frac{VI}{4\pi l} \times \frac{-E_i(\frac{r^2}{4at})}{\Delta\theta(t)}$	 <p>λ(W/(m·K))</p> <p>T(°C)</p> <p>C0S02</p>
Mass loss	 <p>Cubic: L:100mm</p>	 <p>Electric furnace</p> <p>before</p>  <p>m₀</p> <p>after</p>  <p>m_T</p> 	$\frac{m_T}{m_0} = \frac{m_0 - m_T}{m_0}$	 <p>m_T/m₀</p> <p>T(°C)</p> <p>C10S02</p>
Specific heat	 <p>Cubic: L:100mm</p>	 <p>Electric furnace</p>  <p>Temperature acquisition instrument</p>  <p>Temperature curves</p>	<p>Optimization</p>  <p>FEA</p>	 <p>c(J/(kg·K))</p> <p>T(°C)</p> <p>C20S02</p>
Thermal expansion	 <p>Cylinder: Φ 50mm H:100mm</p>	 <p>quartz rod steel shield sample quartz base</p> <p>Furnace chamber Continuous graded heating</p> 	$\varepsilon = \frac{\Delta L}{L}$	 <p>ε(10⁻³)</p> <p>T(°C)</p> <p>C30S02</p>

Figure 2 Principle and flow chart of thermal test

Figure 2 summarizes the above thermal tests, including the size of specimen, test set-up, heating mode, calculation method and test results carried out in this research. Details of the instruments used in the above tests can be found in the literature [31]. The steel shield outside the sample in the heating chamber is to make the sample heated more evenly, which reduces concrete bursting, and for safety protection.

3 Experimental observations

3.1 Macro morphology

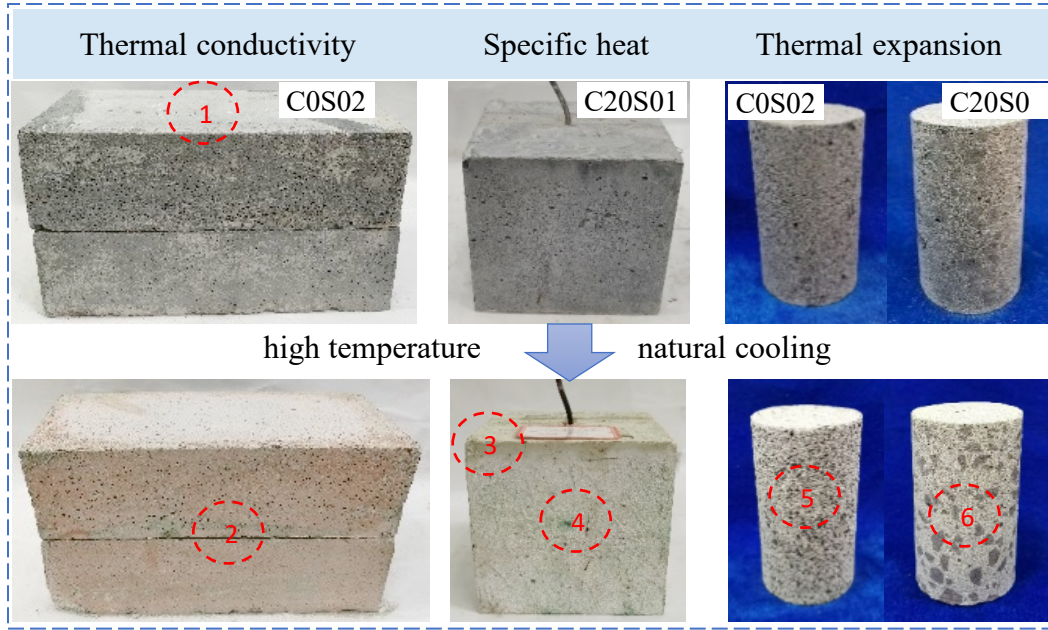
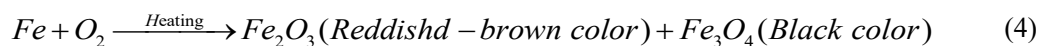
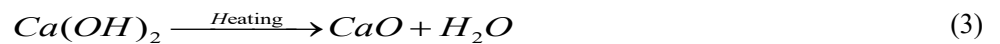
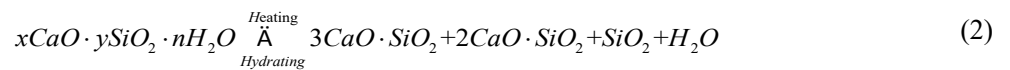


Figure 3 Comparison of sample morphology before and after high temperature: 1. Hydrate covered on the surface before high temperature; 2. Warped in the middle; 3. Crisp of the corners; 4. Some light green on the surface; 5. Steel fibers discoloration; 6. Coarse aggregates discoloration.

Before the test, the upper and lower surfaces of the sample used in the thermal conductivity test appear smooth and compact (Figure 3(①)). Although the side of the sample is not as smooth as the top and bottom surfaces due to the use of wooden mold, the sounds of typing on the sample is clear and loud, indicating a dense structure, i.e, higher thermal conductivity and mass. After exposure to heat, a change of morphology of the sample is evident. The surface color of the sample becomes light green(Figure 3(④)). This is due to the dispersion of the basic copper carbonate generated from copper-plated steel fibers on the surface of the sample (Eq.(1)). Gently removing the surface copper carbonate shows pinkish white subsurface that has a similar color to the color inside the sample. The reason for this phenomenon is that the calcium silicate hydrate (C-S-H) and calcium hydroxide (C-H) in the sample are almost completely decomposed and white calcium oxide (CaO) is then produced (Eq.(2) and Eq.(3)). The decomposition of C-S-H and C-H causes decrease of thermal conductivity and mass loss. Additionally, since the sample is heated over a period of time, iron is oxidized at high temperature to produce iron oxide (Eq.(4)). The white CaO together with a small amount of reddish-brown Fe_2O_3 make the sample an overall pinkish-white color.

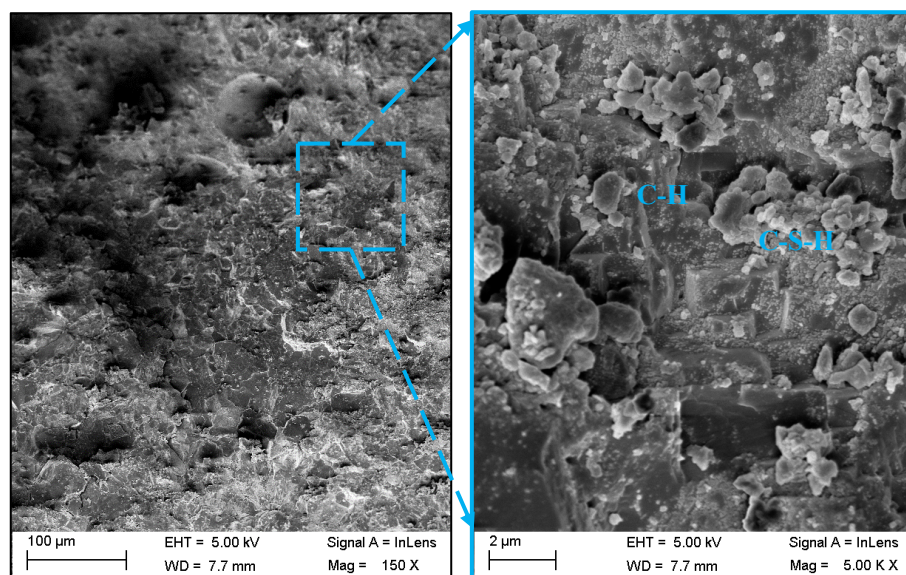


Meanwhile, other manifest changes have also taken place. The sample is crisped as a whole, surface cracks appear along the outer contour of steel fibers and the cement matrix at the corners peels off (Figure 3(③)). The sample warps around the contact of the two samples, so that they no longer fit closely (Figure 3(②)). This can be explained by the chemical decomposition (Eq.(2) and Eq.(3)) and the incompatible deformation of the samples. The pore structure of the sample is coarsened, and the typing sound is low, which indicate that irreversible pores and cracks have been produced from high temperature, resulting in reduction in thermal conductivity and mass and a change in the specific heat of the sample. After 3 days in the air, the sample becomes powdery, which is due to water swelling of CaO (Eq.(5)). The morphological changes of the sample in the specific heat test are consistent with the changes in the thermal conductivity test.

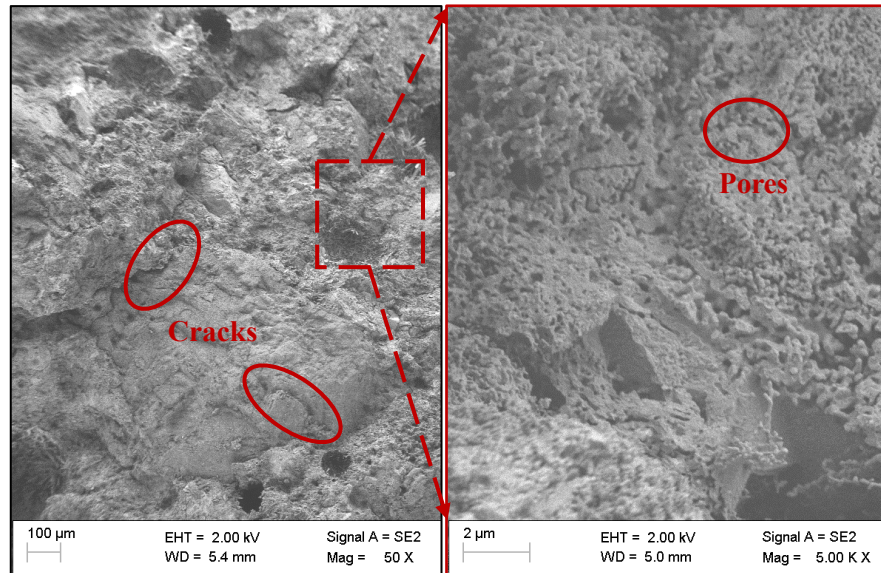


In the thermal expansion test, the color of cement matrix becomes pinkish white, and the color of coarse aggregates change from dark black to reddish brown and then to tan (Figure 3(⑤ and ⑥)). The steel fibers change from the original silvery white to black due to oxidation (Fe_3O_4 in Eq.(4)), and becomes brittle and easy to break. There are net-like micro-cracks distributed on the surface of the sample, especially at both ends of the cylindrical sample, which attributes to the increase of thermal expansion.

3.2 Micro morphology



(a) Morphology at room temperature



(b) Morphology after high temperature

Figure 4 Micro morphology of CA-UHPC before and after high temperature

The micro morphological changes of the sample before and after being subjected to high temperature are studied using field emission scanning electron microscope (FE-SEM) as shown in Figure 4. Before being heated, the compact surface is observed with 150x magnification (Figure 4 (a)). When the magnification is 5000x, the hardened matrix and the complete hydrate can be seen, which shows C-S-H as a three-dimensional network structure composed of nano particles. Inside the CA-UHPC, C-S-H presents irregular spherical particles, and C-H presents a lamella crystal structure. C-S-H is formed closely on the surface of C-H. The formation of hydrates results in a dense structure inside the material, which helps to increase the thermal conductivity and mass of the CA-UHPC. After the sample has experienced high temperature, when the magnification is 50x, obvious cracks and holes are seen (Figure 4 (b)). When the magnification is 5000x, many small pores can be seen between the structures, which is due to the decomposition of hydrates occurring at the meso level, as described in Eq.(2) and Eq.(3). The cluster-like dense structure disappears completely, and the layered C-H is no longer visible. The whole structure has a relatively loose three-dimensional structure. As a result, a fraction of the solids within the material is replaced by pores after the high temperature, which presents a lower thermal conductivity and mass. In addition, the generation of pores and cracks also affects the specific heat and thermal expansion of the material.

4 Test results and analysis

UHPCs of seven different mix ratios are tested for the thermal experiments. Three or four samples of the same mix ratios are, respectively, made and tested for each of the properties, and the results are generally consistent. Thus, 28 (4×7) samples are made for testing thermal conductivity, 21 (3×7) samples are made, respectively, for the specific heat and thermal expansion tests, and a total of 126 (3×7×6) samples are made for the mass loss test as the results are taken at 6 different temperatures. Averages are taken from every group of the

three or four samples with the same mix ratio. To further explore the effect of the coarse aggregate and steel fiber content on the thermal performance of the CA-UHPC, bar charts are plotted in Figure 5 and Figure 6 to show the thermal properties across the range of temperature, where the samples with fixed amounts of coarse aggregates and steel fibers are studied, respectively.

4.1 The influence of coarse aggregates on thermal performance

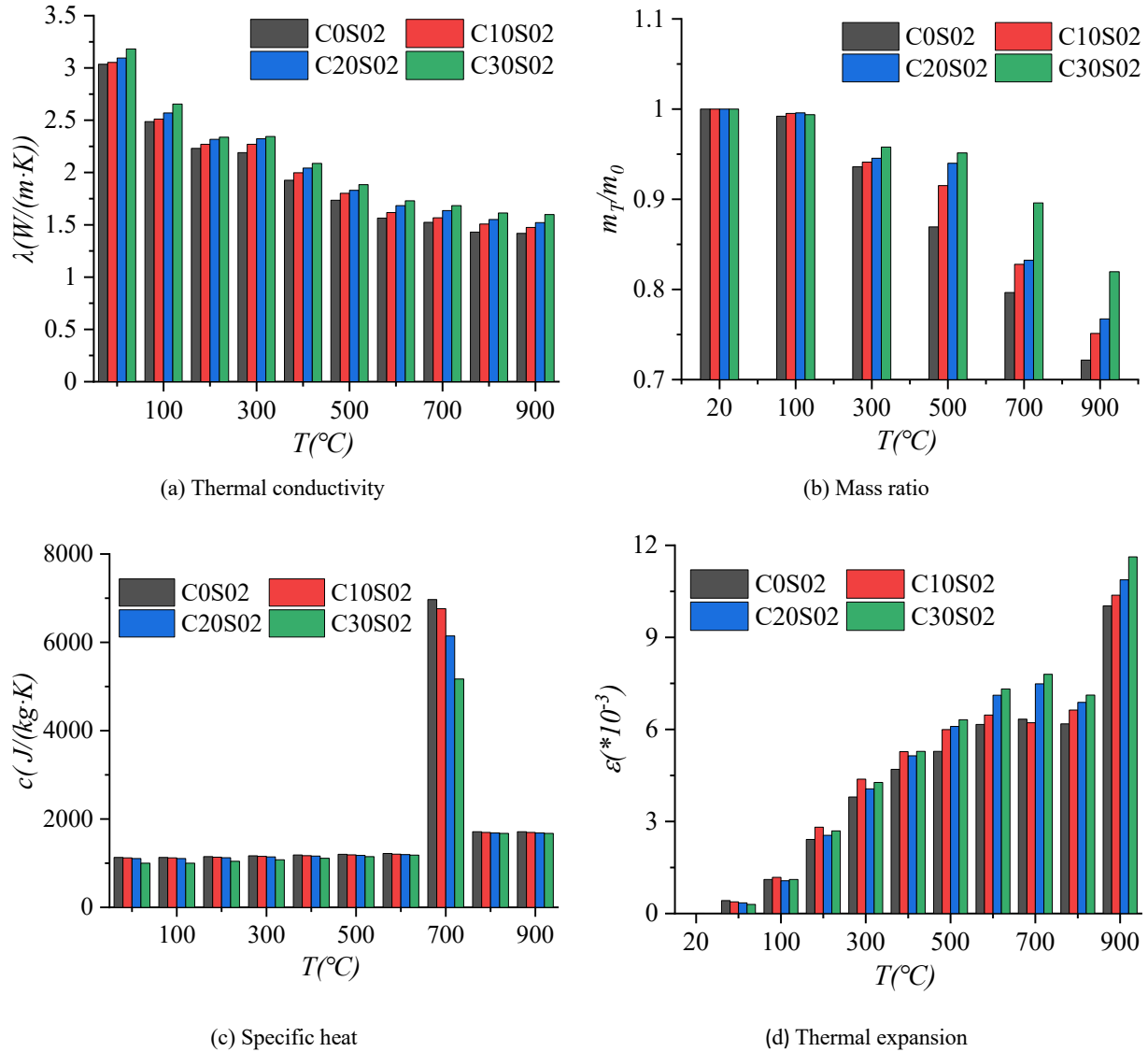


Figure 5 Thermal parameters with coarse aggregate content

Figure 5 presents the influence of coarse aggregates on the thermal parameters, where the content of steel fibers is fixed to 2% in volume. It can be seen that thermal conductivity, mass ratio and thermal expansion of the CA-UHPC are greater when the content of coarse aggregate is higher, while specific heat is negatively related to the volume ratio of coarse aggregates.

When the temperature is below 300 °C, the volume ratio of coarse aggregate has little influence on the thermal properties. Especially for the samples with the content of coarse aggregate less than 20%, the difference of thermal conductivity caused by coarse aggregate content is about 3%. In this temperature range,

the microstructure of internal pores and cracks is virtually unchanged and the small variations of the thermal properties are mainly due to evaporation of free water and hydration reaction, which is not significantly related to the content of coarse aggregate. After 300°C, the influence of the volume ratio on thermal conductivity, mass ratio and thermal expansion becomes greater, as shown in Figure 5(a), (b) and (d). In detail, the thermal conductivity of C30S02 is 5% and 13%, respectively, higher than that of C0S02 at room temperature and 900 °C. This comparison is consistent with the general observation that thermal conductivity increases with the increase of coarse aggregate content. The water content of the CA-UHPC is low, so there is no phenomenal contrast in specific heat at the early stage of heating.

The specific heat and thermal expansion have the largest difference at 700°C due to the difference in coarse aggregate content (Figure 5(c) and (d)), where the specific heat of C30S02 decreases by 26% and the thermal expansion increases by 23% when compared, respectively, with those of C0S02. Because when the temperature reaches 700°C, the decomposition rate of hydrate reaches a peak again. The increase of coarse aggregate content results in reduction in hydrate content and the heat absorbed by the decomposition reaction, hence a lower specific heat. Similarly, the thermal expansion of the samples containing more coarse aggregate is smaller due to less hydrate content.

When the temperature reaches 900°C, as shown in Figure 5(a) and (b), the thermal conductivity is reduced by about 50%, and the mass reduction ranges from 18% to 28%. Compared with at room temperature, at 900°C the difference between the CA-UHPCs becomes more apparent, as the materials have deteriorated to different extend due to their different coarse aggregate content. At this temperature, the pores are severely coarsened, and more cracks are connected with each other, which reduces the overall thermal conductivity and mass of the samples. Hence, a sample with more coarse aggregate content will have higher thermal conductivity and mass. At this stage, all the chemical bound water has been completely lost, resulting in little change in the specific heat, and the expansion of coarse aggregates and the development of macroscopic cracks allow for a rapid increase in thermal expansion. In general, coarse aggregates exhibit higher thermal conductivity, residual mass and thermal expansion and deteriorates less than matrix does, which has a great impact on the thermal performance of CA-UHPC.

4.2 The influence of steel fiber on thermal performance

The thermal properties of the CA-UHPC with different steel fiber contents are plotted in Figure 6, where the coarse aggregate content of the mixture is fixed at 20%.

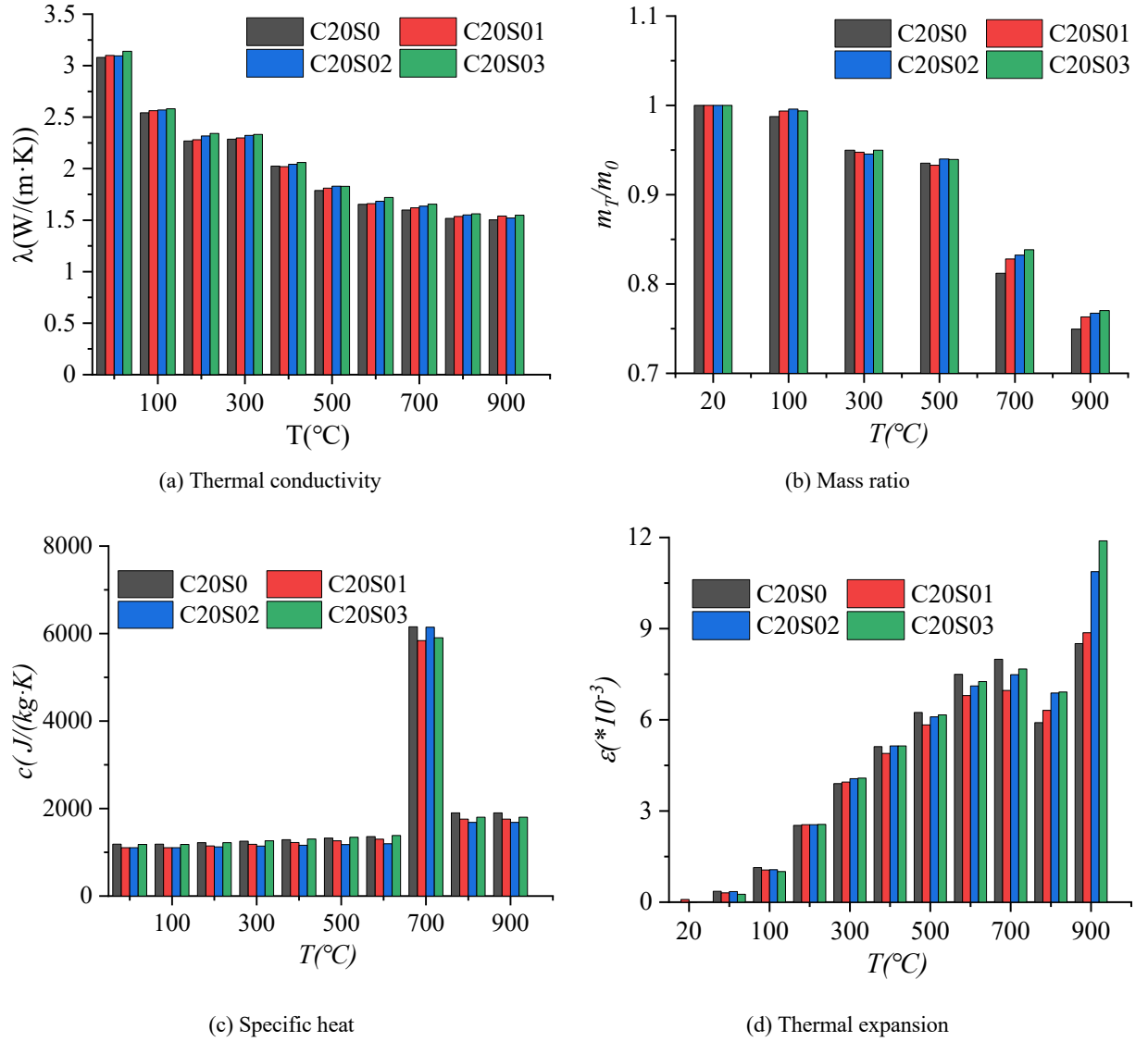


Figure 6 Thermal parameters with steel fiber content

The thermal conductivity of steel is about $53\text{W}/(\text{m}\cdot\text{K})$, which is significantly higher than that of cement concrete. Theoretically, a larger proportion of steel fibers in concrete results in greater thermal conductivity of the material. Figure 6 (a) exhibits that steel fibers can increase the thermal conductivity, but only marginally when the content of steel fibers increases from 0 to 3%, which was also observed in other literatures^[35]. The introduction of steel fibers slightly increases the porosity of the concrete, which results in a reduction in thermal conductivity and offsets any increase in the thermal conductivity of the samples due to the addition of steel fibers. The percentage volume difference of steel fibers in the CA-UHPC brings only a small overall difference in the mass ratio of the material. For every 1% increase of steel fibers, the mass difference is within 2%. At 900°C , the reduction of mass of the CA-UHPC is between 23% and 25%, as shown in Figure 6 (b) when compared with the mass at 20°C . Similarly, the effect of steel fiber content on specific heat is not significant, as shown in Figure 6(c).

The effect of steel fibers on thermal expansion mainly starts noticeably at 400°C as shown in Figure 6 (d).

The coefficient of linear expansion of steel fibers is close to that of concrete. Steel fibers also have inhibitory effect on inside crack propagation. Therefore, thermal expansion of the samples without steel fibers is larger, and the thermal expansion of C20S01 is minimum between 400°C~700°C. However, at 800°C~900°C, thermal expansion increases as the increase of steel fiber content, i.e., $C20S0 < C20S01 < C20S02 < C20S03$. This is because at high temperature the steel fibers are softened and the crack suppression effect is weakened. Many macro- and micro-cracks in the CA-UHPC are observed (Figure 3), and significant thermal expansion is evident.

In summary, the influence of steel fibers on thermal performance is not as obvious as that of coarse aggregates. And since the steel fiber content is less than 3%, the influence of steel fibers can be ignored.

4.3 The influence of temperature on the thermal properties.

With the increase of temperature, the thermal properties of all the samples show the same upward or downward patterns (Figure 5 and Figure 6). In Figure 5(a) and Figure 6(a), the thermal conductivity decreases as the temperature increases from room temperature to 200°C, a slightly increase when the temperature is from 200°C to 300°C, and then decreases continuously after 300°C. When the temperature reaches 800°C ~900°C, the decrease of thermal conductivity tends to be small. The thermal conductivity varies between 1.42 W/(m·K) ~ 3.18 W/(m·K).

The loss of mass reflects the reduction of water and compounds. The mass loss increases with the increase of temperature, and is accelerated after 500°C, as plotted in Figure 5(b) and Figure 6(b). The mass ratio varies between 0.72 ~ 0.82 at 900°C. Figure 5(c) and Figure 6(c) show that the specific heat is almost unchanged from room temperature to 600°C, rises sharply between 600°C~700°C, and then falls dramatically between 700°C ~800°C. From 20°C to 700°C, the thermal strain increases monotonically, as shown in Figure 5(d) and Figure 6(d), where the thermal strain increases approximately linearly between 20°C ~300°C. The sample continues to expand when it is heated from 300°C ~700°C, but the expansion rate is substantially lower than that in the previous stage. The thermal strain shows a sharp decline and then a sharp rise between 700°C~800°C and 800°C~900°C, respectively.

The above observations can be explained further by studying the change of microstructures of the samples at different stages of heating. From 100°C to 300°C, the free water inside the sample evaporates, and a space of vapor pressure is developed internally within the CA-UHPC. In this heating stage, rehydration produces more C-S-H and C-H that fill some existing pores and the pores occupied originally by free water. As a result, the thermal conductivity increases slightly at 300°C, as shown in Figure 5(a) and Figure 6(a). The heat changes caused by free water evaporation and hydration are partly mutual compensating, so that the change of specific heat is not apparent (Figure 5(c) and Figure 6(c)). However, due to the high thermal expansion of the cement

matrix paste and the aggregates^[17], the thermal expansion curve in Figure 5(d) and Figure 6(d) is approximately straight upward.

From 300°C to 700°C, thermal stress increases, damage occurs inside the structure and microcracks begin to appear. At 500°C, significant hydrate decomposition occurs, most of the internal bound water loses and the pore structure coarsens. At 573°C, the quartz sand undergoes an allotropic transformation from α to β quartz, accompanied by nearly 0.85% volume expansion^[32]. As the temperature continues to rise, the decomposition reaction intensifies. At this heating stage, thermal conductivity exhibits a continuous downward trend (Figure 5(a) and Figure 6(a)). Thermal expansion continues to increase, while the expansion rate is significantly lower than that of the previous stage (Figure 5(d) and Figure 6(d)).

From 700°C to 900°C, the internal hydrate decomposition rate reaches another peak at 700°C^[33], and the decomposition process is endothermic. The austenitization of steel at about 750°C absorbs massive amount of heat and causes a substantial reduction in the volume of the steel.^[34], though this reduction is not significant in the samples, due to the low content of steel fibers. The decomposition process absorbs a significant amount of heat, which makes the specific heat increase sharply to the peak value in Figure 5(c) and Figure 6(c). The volume shrinkage caused by steel fiber phase transformation and the expansion of steel fibers caused by thermodynamics roughly offset each other, but the shrinkage caused by decomposition is clearly seen in Figure 5(d) and Figure 6(d) as an overall reduction of thermal expansion at 800°C. After this stage, the cracks incurred from the incompatibility between the shrinkage of the cement matrix and the expansion of the coarse aggregates develop further, as shown in Figure 4 (b). Larger cracks are clearly visible on the surface of the samples (Figure 3), which are accompanied by large volume expansion. In this stage, Figure 5 and Figure 6 show that the thermal conductivity decreases slowly, the specific heat reaches the peak, and the thermal expansion increases sharply after a decline before 800°C.

5 Meso-scale analytical formulas for estimating thermal properties of CA-UHPC at high temperatures

It is known from the above studies that the effect of steel fibers on the thermal performance of CA-UHPC is very small and can be ignored, when the steel fiber content is small (less than 3%). Thus, to develop simple analytical formulas with acceptable accuracy, CA-UHPC can be regarded as a two-phase material composed of coarse aggregates and matrix only.

5.1 Thermal conductivity at high temperatures

The two-phase basic models for calculating thermal conductivity include parallel model, series model and Maxwell model, as shown, respectively^[12] in Eqs.(6)~(8)

$$\lambda = \lambda_M V_M + \lambda_C V_C \quad (6)$$

$$\lambda = \frac{1}{V_M / \lambda_M + V_C / \lambda_C} \quad (7)$$

$$\lambda = \lambda_M \frac{\lambda_C + 2\lambda_M + 2v_C(\lambda_C - \lambda_M)}{\lambda_C + 2\lambda_M - v_C(\lambda_C - \lambda_M)} \quad (8)$$

where, λ is thermal conductivity of CA-UHPC. λ_M and λ_C represent the thermal conductivity of matrix and coarse aggregates, respectively. V_M and V_C are the volume fraction of matrix and coarse aggregates, respectively. The parallel and series models provide, respectively, the upper and lower limits of the property^[36].

To facilitate engineering applications, the test values (Figure 5(a)) of the matrix are fitted to obtain the temperature dependent relationship in Eq.(9)

$$\lambda_M(T) = 2 \times 10^{-6} T^2 - 0.0035T + 2.9631 \quad (9)$$

The thermal conductivity of coarse aggregates at different temperatures can be calculated using the empirical formula (Eq.(10)) given by Zoth and Hane^[37]:

$$\lambda_C(T) = \frac{A}{(350 + T)} + B \quad (10)$$

where A and B are constant coefficients depending on the types of rock. In this paper, artificially broken basalt is selected, taking $A=718$ and $B=1.47$ by fitting the test data in Figure 5(a) to obtain the thermal conductivity formula of coarse aggregates (Eq.(11)):

$$\lambda_C(T) = \frac{718}{(350 + T)} + 1.47 \quad (11)$$

The thermal conductivities calculated from the three models, respectively, using Eq.(6)~(8) are all close to the experimental value with comparable accuracy. Hence, the simplest parallel model is selected and used in the calculations below.

Figure 7 shows the comparisons between the test results (Figure 5(a)) and the results predicted by Eq.(6). It can be seen that the calculation results are in good agreement with the test results, and the difference is within a $\pm 10\%$ error band.

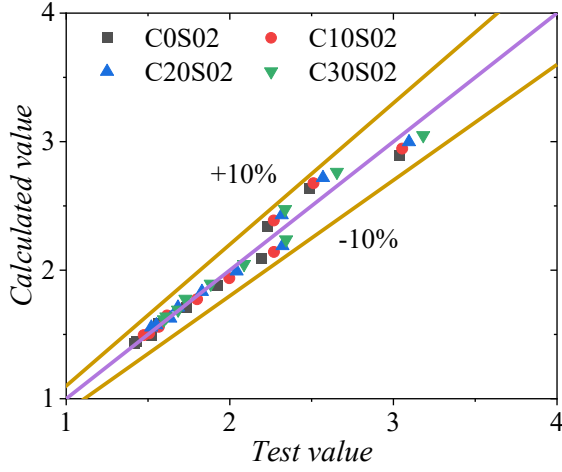


Figure 7 Comparison of calculated and test values of thermal conductivity

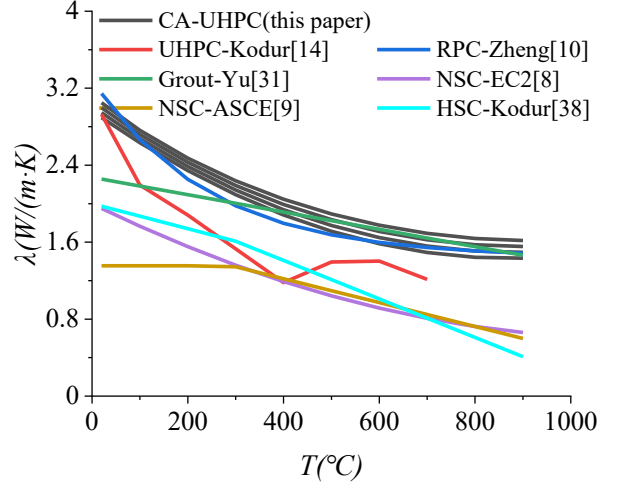


Figure 8 Thermal conductivity of different cement-based materials

Figure 8 shows the thermal conductivity curves of Kodur^[14, 38], Zheng^[10], Yu^[31], EC2^[8] and ASCE^[9] for UHPC, RPC, Grout, HSC, NSC and this paper for comparisons. As can be seen from the figure, in general, thermal conductivity decreases as temperature increases. The thermal conductivities of these cement-based materials can be divided into three categories. The first one includes NSC and HSC. The thermal conductivities of NSC(EC2) and HSC (Kodur) are close to each other at room temperature, and the thermal conductivities of NSC(EC2) and NSC(ASCE) are almost the same after 300°C. As the temperature increases, the thermal conductivity of HSC decreases the fastest. The second category is grout. Its thermal conductivity decreases linearly, and the overall thermal conductivity is 0.3~1.1 W/(m·K) higher than that of HSC. The third category includes RPC, UHPC and CA-UHPC. Their thermal conductivities are close at room temperature, but the thermal conductivity of UHPC changes rapidly, while that of RPC and CA-UHPC change rather slowly, as the temperature increases. The thermal conductivity of RPC decreases faster than CA-UHPC does in the early stage of heating, but becomes slower in the later stage. The reduction rate in thermal conductivity of CA-UHPC is smaller than that of RPC, due to the addition of coarse aggregates.

5.2 Mass ratio and specific heat at high temperatures

5.2.1 Mass ratio

The experimental data (Figure 5(b)) at high temperatures are fitted to obtain the relationship between the mass ratio of the matrix and the temperature, as follows

$$\frac{m_{MT}}{m_{M0}}(T) = -0.00032T + 1.023 \quad (12)$$

In Eq.(12), m_{MT} and m_{M0} denote, respectively, the mass of cement matrix at temperature T and room temperature.

The mass ratio of coarse aggregates at high temperatures is calculated by referring to the formula given in [39],

$$\frac{m_{CT}}{m_{C0}}(T) = \begin{cases} 1, & T \leq 400^\circ\text{C} \\ 1 + (1.88 - 0.6 \times \ln(T - 350.5)) / 100, & 400^\circ\text{C} < T \leq 1000^\circ\text{C} \end{cases} \quad (13)$$

where m_{CT} and m_{C0} are, respectively, the mass of matrix at temperature T and room temperature.

Eq.(14) is the parallel model for the mass ratio of CA-UHPC with different amounts of coarse aggregates

$$\frac{m_T}{m_0} = \frac{m_{MT}}{m_{M0}} V_M + \frac{m_{CT}}{m_{C0}} V_C \quad (14)$$

Figure 9 compares the calculated values of Eq.(14) with the test values (Figure 5(b)), which shows that they are well correlated and is within a $\pm 5\%$ error band.

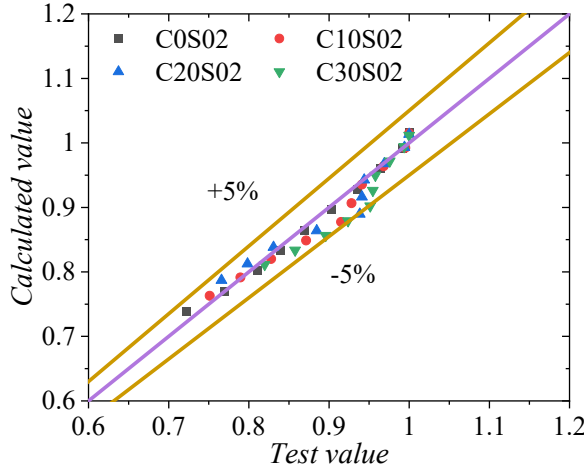


Figure 9 Comparison of calculated and test values of mass ratio

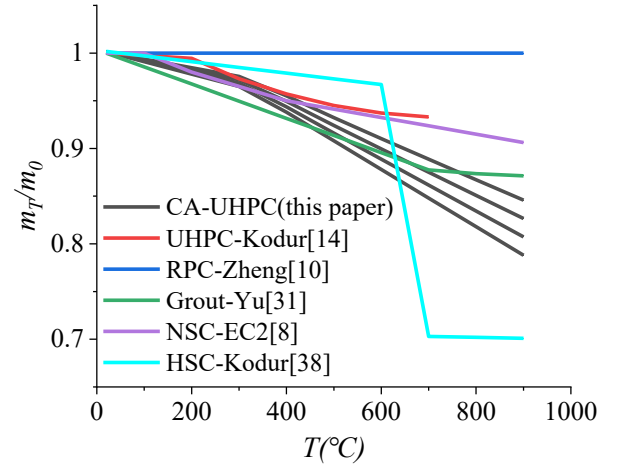


Figure 10 Mass ratio of different cement-based materials

The mass ratios of UHPC^[14], RPC^[10], Grout^[31], HSC^[38], NSC^[8] and CA-UHPC are shown in Figure 10. Except for PRC that was assumed constant in the reference^[10], the mass ratios of other cement-based materials decrease with the increase of temperature. Before 400°C, the mass ratio reduction rate of CA-UHPC is close to that of UHPC and NSC. However, after 400°C, the mass ratio reduction rate of CA-UHPC accelerates. The mass loss of CA-UHPC is between Grout and HSC when the temperature reaches 900°C.

5.2.2 Specific heat

Eq.(15) is the specific heat of the matrix obtained from fitting the experimental data of C0S02 (Figure 5(c)).

$$c_M = \begin{cases} 0.156T + 1127.2, & 20^\circ\text{C} \leq T \leq 600^\circ\text{C} \\ 57.49T - 33274, & 600^\circ\text{C} < T \leq 700^\circ\text{C} \\ -35.49T + 31812, & 700^\circ\text{C} < T \leq 800^\circ\text{C} \\ 1710, & 800^\circ\text{C} < T \leq 900^\circ\text{C} \end{cases} \quad (15)$$

where c_M is the specific heat of the matrix.

The specific heat of coarse aggregates is calculated by Eq.(16) from Zhang^[40]:

$$c_C = 625(1 + T)^{0.075} \quad (16)$$

where c_C is the specific heat of coarse aggregates.

By using the parallel model, the specific heat of CA-UHPC with different coarse aggregate contents at different temperatures can be calculated as follows:

$$c = c_M V_M + c_C V_V \quad (17)$$

Figure 11 is the comparison between the test values (Figure 5(c)) and the calculated results of Eq.(17), where good agreement with the test results is observed, and most of the error is within $\pm 10\%$.

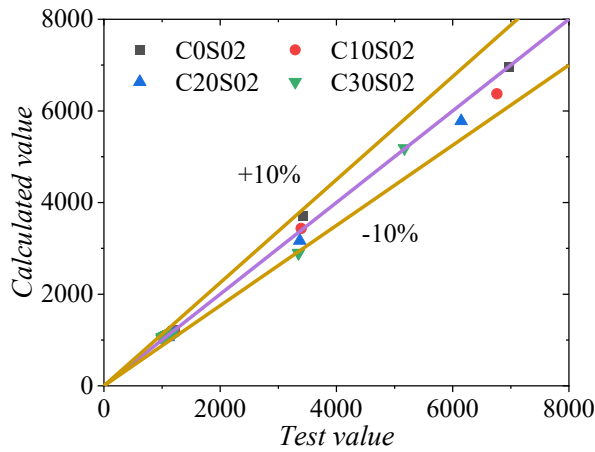


Figure 11 Comparison of calculated and test values of specific heat

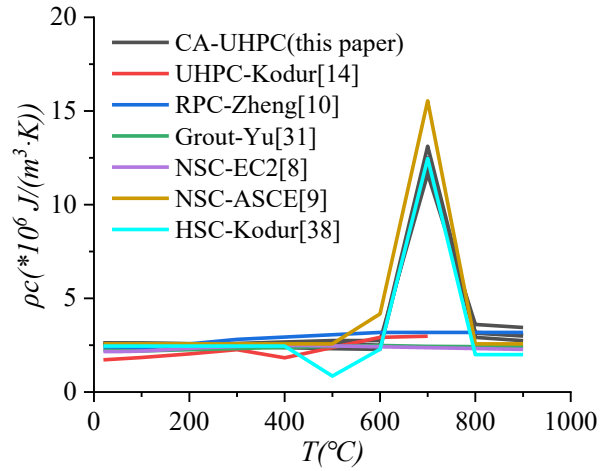


Figure 12 Heat capacity curves of different cement-based materials

Heat capacity can be expressed as the product of specific heat and density. The high-temperature heat capacity curves of Kodur^[14, 38], Zheng^[10], Yu^[31], EC2^[8], ASCE^[9] and this paper are plotted in Figure 12. It can be seen that the trend of the heat capacity curve of CA-UHPC is similar to that of NSC and HSC, and the peak value of CA-UHPC at 700°C is close to that of HSC. The heat capacity decreases dramatically between 700°C~800°C, indicating that heat absorption is phenomenal within this range.

5.3 Thermal expansion at high temperatures

The fitted equations of thermal strains of the matrix (Figure 5(d)) are,

$$\varepsilon_M(T)=\begin{cases} 1.35\times 10^{-3}T-0.027, & 20^{\circ}\text{C}\leq T\leq 300^{\circ}\text{C} \\ -1.0\times 10^{-6}T^2+1.7\times 10^{-3}T-0.073, & 300^{\circ}\text{C}<T\leq 700^{\circ}\text{C} \\ 2.0\times 10^{-5}T^2-3.01\times 10^{-2}T+11.9, & 700^{\circ}\text{C}<T\leq 900^{\circ}\text{C} \end{cases} \quad (18)$$

where ε_M is the thermal strain of the matrix.

Based on the homogenization theory and the mixture model, the thermal expansion of coarse aggregate can be inversely fitted from the test data (Figure 5(d)),

$$\varepsilon_C(T)=1.6\times 10^{-3}T-0.032 \quad (19)$$

where ε_C is the thermal strain of coarse aggregate.

Eq.(20) combines the matrix and coarse aggregates using the mixture model^[41] to obtain the calculation formula for the thermal strain of CA-UHPC with different coarse aggregate contents at different temperatures

$$\varepsilon=\varepsilon_M V_M + \varepsilon_C V_C \quad (20)$$

Comparing the predicted strains calculated from Eq.(20) with the experimental values (Figure 5(d)) in Figure 13, it can be seen that except the large deviation of the value at 50°C, the calculation curve is well consistent with the experimental curve.

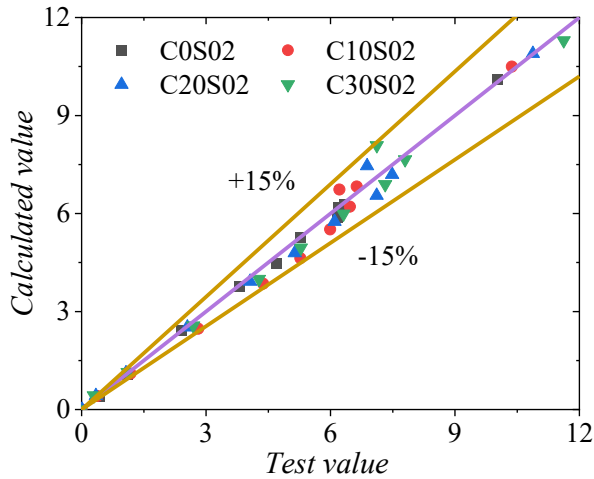


Figure 13 Comparison of calculated and test values of thermal expansion

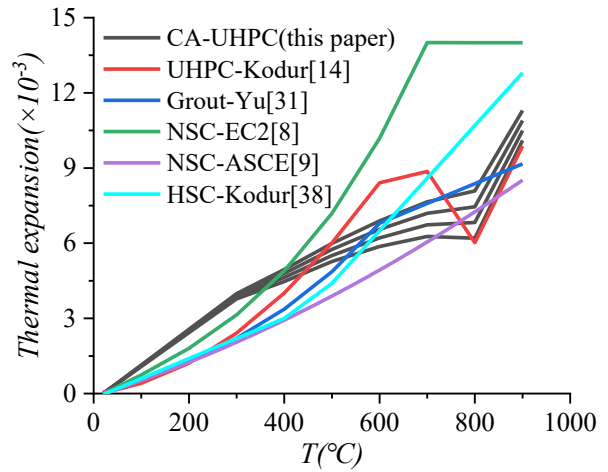


Figure 14 Thermal expansion of different cement-based materials

The high-temperature thermal expansion curves of Kodur^[14, 38], Yu^[31], EC2^[8], ASCE^[9] and this paper are plotted in Figure 14. As a whole, thermal expansion increases with the increase of temperature. The thermal expansion of both UHPC and CA-UHPC show a tendency of decreasing from 700°C to 800°C, which is much more significant for UHPC. This can be explained by the fact that they all contain more cementitious materials than the other four materials. The decomposition of more hydrates at this temperature range are the main factor causing reduction in the thermal expansion.

6 Conclusion

This paper studied some of the most important thermal properties, including thermal conductivity, mass loss, specific heat and thermal expansion, of CA-UHPC at high temperatures. Experiments were conducted to measure the properties and simple analytical formulas were proposed for potential adoption by structural and material engineers. The following conclusions were drawn from the study.

- (1) High temperature has a considerable influence on the morphological characteristics of CA-UHPC, such as change of the color and percussion sound, structure crispness, network cracks, etc. At the micro level, the reduction of hydrate, interface crack and pores coarsening can be observed.
- (2) In general, thermal conductivity of CA-UHPC decreases with the increase of temperature, which is almost plateaued around 300°C due to the further hydration of CA-UHPC in the vapor pressure environment. The mass ratio keeps decreasing with the increase of temperature. The specific heat and thermal expansion increase as the temperature rises, which is more prominent between 700°C and 800°C. This is because the decomposition rate of hydrate reaches a peak at about 700°C, and the steel fibers undergo austenite transformation, which makes CA-UHPC absorb more heat and shrink. It is manifested by a rapid rise in specific heat and a decline in thermal expansion, respectively, before and after 700°C.
- (3) Coarse aggregates attribute to the increase of thermal conductivity, mass ratio and thermal expansion of CA-UHPC, and decrease of the specific heat. Especially CA-UHPC with 30% coarse aggregates has the most manifest effect. However, the influence of steel fibers on thermal performance is not as obvious as coarse aggregates. Adding more coarse aggregates to CA-UHPC can reduce the overall cost, but it will increase the thermal conductivity and thermal expansion of the material. This requires finding a right balance that is most suitable for a design.
- (4) The simple formulas for predicting the temperature dependent thermal properties of CA-UHPC with varying coarse aggregate contents can provide estimate of the properties with satisfactory agreement with the experimental results, which can be used next in simulating temperature field and coupled temperature-mechanical effect within structural components made of CA-UHPC.
- (5) Compared with the cement-based materials such as UHPC and RPC, thermal conductivity of CA-UHPC is higher with a smaller reduction rate. The mass loss is more significant, and the specific heat and thermal expansion changes more dramatically around 700°C.

Acknowledgements

The authors are grateful for the financial support from the National Natural Science Foundation of China (Grant No. 51878518, 51738011) and China Scholarship Council (202006270175).

References

- [1] Asadi I, Shafigh P, Hassan Z F B A, et al. Thermal Conductivity of Concrete– a Review[J]. Journal of Building Engineering, 2018:81-93.
- [2] Malik M, Bhattacharyya S K, Barai S V. Thermal and Mechanical Properties of Concrete and its Constituents at Elevated Temperatures: A Review[J]. Construction and Building Materials, 2020:121398.
- [3] Wang W, Wang H, Chang K, et al. Effect of High Temperature on the Strength and Thermal Conductivity of Glass Fiber Concrete[J]. Construction and Building Materials, 2020,245:118387.
- [4] Li X, Bao Y, Wu L, et al. Thermal and Mechanical Properties of High-Performance Fiber-Reinforced Cementitious Composites After Exposure to High Temperatures[J]. Construction and Building Materials, 2017,157:829-838.
- [5] Wang W, Lu C, Li Y, et al. An Investigation on Thermal Conductivity of Fly Ash Concrete After Elevated Temperature Exposure[J]. Construction and Building Materials, 2017,148:148-154.
- [6] Zhang Y, Sun Q, Yang X. Changes in Color and Thermal Properties of Fly Ash Cement Mortar After Heat Treatment[J]. Construction and Building Materials, 2018,165:72-81.
- [7] Ju Y L H L. Investigation on Thermophysical Properties of Reactive Powder Concrete[J]. Science and technology in China, 2011,54(12):3382-3403.
- [8] Eurocode 2: Design of Concrete Structures-Part 1-2:General Rules-Structural Fire Design[S]. Brussels: CEN[S]. 2004.
- [9] Structural Fire Protection[S]. New York, USA: 1992.
- [10] Zheng W, Wang R, Wang Y. Experimental study on thermal parameter of reactive powder concrete [J]. Journal of Building Structures. 2014,35(09):107-114.
- [11] Kim K, Jeon S, Kim J, et al. An Experimental Study On Thermal Conductivity of Concrete[J]. Cement and Concrete Research, 2003,33(3):363-371.
- [12] Zhang W, Min H, Gu X, et al. Mesoscale Model for Thermal Conductivity of Concrete[J]. Construction and Building Materials, 2015,98:8-16.
- [13] Corinaldesi V, Moriconi G. Mechanical and Thermal Evaluation of Ultra High Performance Fiber Reinforced Concretes for Engineering Applications[J]. Construction and Building Materials, 2012,26(1):289-294.
- [14] Kodur V, Asce F, Banerji S, et al. Effect of Temperature on Thermal Properties of Ultrahigh-Performance Concrete[J]. Journal of Materials in Civil Engineering, 2020,32(8).
- [15] Kodur V K R, Sultan M A. Effect of Temperature on Thermal Properties of High-Strength Concrete[J]. Journal of Materials in Civil Engineering, 2003,15(2):101-107.
- [16] Kodur V. Properties of Concrete at Elevated Temperatures[J]. International Scholarly Research Notices, 2014:1-15.
- [17] Khaliq W, Kodur V. Thermal and Mechanical Properties of Fiber Reinforced High Performance Self-Consolidating Concrete at Elevated Temperatures[J]. Cement and Concrete Research, 2011,41(11):1112-1122.
- [18] Emanuel J H, Hulsey J L. Prediction of the Thermal Coefficient of Expansion of Concrete[J]. Journal Proceedings, 1977,74(4).

- [19] Siddiqui M S, Fowler D W. A Systematic Optimization Technique for the Coefficient of Thermal Expansion of Portland Cement Concrete[J]. Construction and Building Materials, 2015,88:204-211.
- [20] Nahhas T, Py X, Sadiki N. Experimental Investigation of Basalt Rocks as Storage Material for High-Temperature Concentrated Solar Power Plants[J]. Renewable and Sustainable Energy Reviews, 2019,110:226-235.
- [21] Vigroux M, Eslami J, Beaucour A, et al. High Temperature Behaviour of Various Natural Building Stones[J]. Construction and Building Materials, 2021,272:121629.
- [22] Zhao D, Qian X, Gu X, et al. Measurement Techniques for Thermal Conductivity and Interfacial Thermal Conductance of Bulk and Thin Film Materials[J]. Journal of Electronic Packaging, 2016,138(4).
- [23] Dos Santos W N. Effect of Moisture and Porosity on the Thermal Properties of a Conventional Refractory Concrete[J]. Journal of the European Ceramic Society, 2003,23(5):745-755.
- [24] Gomes M G, Flores-Colen I, Da Silva F, et al. Thermal Conductivity Measurement of Thermal Insulating Mortars with EPS and Silica Aerogel by Steady-State and Transient Methods[J]. Construction and Building Materials, 2018,172:696-705.
- [25] H G W. The Determination of Transient Temperatures and Heat Transfer at a Gas-Metal Interface Applied to a 40-Mm Gan Barrel[J]. Jet Propulsion, 1955,25(4):158-162.
- [26] G S. Numerical Solutions to an Inverse Problem of Heat Conduction for Simple Shaps[J]. ASME Journal of Heat Transfer, 1960,82(1):20-26.
- [27] J H. Lectures on Cauchy's Problem in Linera Differential Equations[M]. New Haven: Yale University Press, 1923.
- [28] Zahabizadeh B, Edalat-Behbahani A, Granja J, et al. A New Test Setup for Measuring Early Age Coefficient of Thermal Expansion of Concrete[J]. Cement and Concrete Composites, 2019,98:14-28.
- [29] Li L, Dao V, Lura P. Autogenous Deformation and Coefficient of Thermal Expansion of Early-Age Concrete: Initial Outcomes of a Study Using a Newly-Developed Temperature Stress Testing Machine[J]. Cement and Concrete Composites, 2021,119:103997.
- [30] Childs P, Wong A C L, Gowripalan N, et al. Measurement of the Coefficient of Thermal Expansion of Ultra-High Strength Cementitious Composites Using Fibre Optic Sensors[J]. Cement and Concrete Research, 2007,37(5):789-795.
- [31] Xue C, Su C, Yu M, et al. Experimental Study on the Thermal-Mechanical Properties and Degradation of Sleeve Grouting Material at Elevated Temperatures[J]. Journal of Materials in Civil Engineering, 2020.
- [32] Johnson W H, Parsons W H. Thermal Expansion of Concrete Aggregate Materials[J]. Journal of Research of the National Bureau of Standards, 1994.
- [33] Fu Y, Wong Y, Poon C, et al. Experimental Study of Micro/Macro Crack Development and Stress–Strain Relations of Cement-Based Composite Materials at Elevated Temperatures[J]. Cement and Concrete Research, 2004,34(5):789-797.
- [34] Yu H, Yu X, Yu C. Structural fire safety design [M]. Beijing: Science Press, 2012:64.
- [35] Kodur V K R, Sultan M. Thermal Properties of High Strength Concrete at Elevated Temperatures: CANMET/ACI/JCI International conference on recent advances in concrete technology, Tokushima,Japan, 1998[C].
- [36] Wang J, Carson J K, North M F, et al. A New Structural Model of Effective Thermal Conductivity for Heterogeneous Materials with Co-Continuous Phases[J]. International Journal of Heat and Mass Transfer, 2008,51(9-10):2389-2397.
- [37] G Z, R H. Handbook of Terrestrial Heat flow Density Determination. [M]. Dordrecht: Kluwer Academic Publishers, 1988.
- [38] Kodur V K R, Sultan M A. Effect of Temperature on Thermal Properties of High-Strength Concrete[J].

Journal of Materials in Civil Engineering, 2003,15(2):101-107.

- [39] Sun W, Jin A, Wang S, et al. Study on sandstone split mechanical properties under high temperature based on the DIC technology [J]. Rock and Soil Mechanics, 2021,42(2):511-518.
- [40] Zhang R, Jin L, Du X. Journal of Beijing University of Technology [J]. Journal of Beijing University of Technology, 2018,44(12):1503-1512.
- [41] Sideridis E. Thermal Expansion Coefficients of Fiber Composites Defined by the Concept of the Interphase[J]. Composites Science and Technology, 1994,51(3):301-317.